Multidimensional super-resolution microscopy unveils nanoscale surface aggregates in the aging of FUS condensates

Changdong He,

Chun Ying Wu,

Wan Li,

Ke Xu[*]

Department of Chemistry, University of California, Berkeley, California 94720, United States.

Abstract

The intracellular liquid-liquid phase separation (LLPS) of biomolecules gives rise to condensates that act as membrane-less organelles with vital functions. FUS, an RNA-binding protein, natively forms condensates through LLPS and further provides a model system for the often disease-linked liquid-to-solid transition of biomolecular condensates during aging. However, the mechanism of such maturation processes, as well as the structural and physical properties of the system, remain unclear, partly attributable to difficulties in resolving the internal structures of the micrometer-sized condensates with diffraction-limited optical microscopy. Harnessing a set of multidimensional super-resolution microscopy tools that uniquely map out local physicochemical parameters through single-molecule spectroscopy, here we uncover nanoscale heterogeneities in FUS condensates and elucidate their evolution over aging. Through spectrally resolved single-molecule localization microscopy (SR-SMLM) with a solvatochromic dye, we unveil distinct hydrophobic nanodomains at the condensate surface. Through SMLM with a fluorogenic amyloid probe, we identify these nanodomains as amyloid aggregates. Through single-molecule displacement/diffusivity mapping (SM*d*M), we show that such nanoaggregates drastically impede local diffusion. Notably, upon aging or mechanical shears, these nanoaggregates progressively expand on the condensate surface, thus leading to a growing low-diffusivity shell while leaving the condensate interior diffusion-permitting. Together, beyond uncovering fascinating structural arrangements and aging mechanisms in the single-component FUS condensates, the demonstrated synergy of multidimensional super-resolution approaches in this study opens new paths for understanding LLPS systems at the nanoscale.
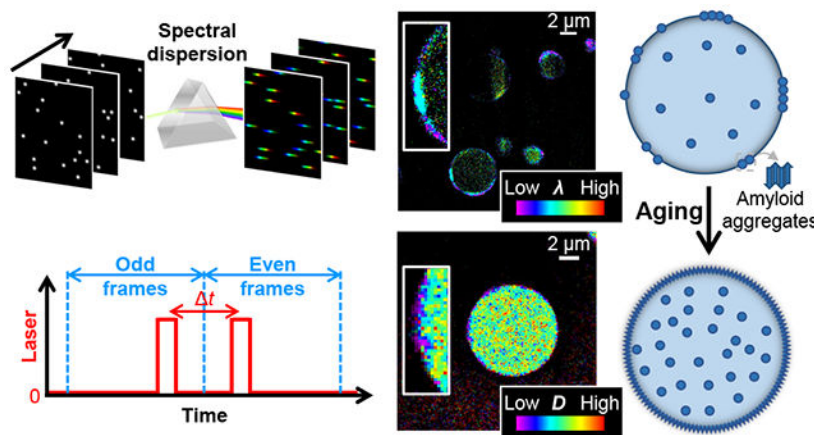
Graphical Abstract

[*]Correspondence to: xuk@berkeley.edu.

Introduction

The past decade has witnessed the fast growth of research on microdroplet-like "condensates" generated and maintained *via* the liquid-liquid phase separation (LLPS) of biomolecules.[1-4] By bringing together relevant molecular players, including proteins and nucleic acids, and modulating local physicochemical parameters, *e.g.*, diffusivity and hydrophobicity, such "membrane-less organelles" give rise to vital cellular functions,[5] *e.g.*, signaling[6,7] and gene control.[8-10]

The RNA-binding protein FUS (fused in sarcoma) and related proteins serve as model systems for LLPS and biomolecular condensates.[11-19] Formed through LLPS owing to intrinsically disordered low-complexity domains, FUS condensates are further known for their gradual transition from an initially liquid state to a solid or glassy state through aging,[11,14,16,19] a process accelerated by mutations linked to neurodegenerative diseases.[11,12,15,18] Related aging/maturation processes have been reported in numerous LLPS systems, including other neurodegenerative-disease players such as hnRNPA1,[20] Tau,[21,22] TDP-43,[23] and α-synuclein.[24] However, the mechanism of such processes, as well as the overall structural and physical properties of the system, remain unclear. For example, for single-component LLPS condensates, whereas it is common to assume that each microdroplet adopts a homogenous phase, recent theoretical and experimental work points to potential intra-condensate inhomogeneity, *e.g.*, the gradual transformation of FUS LLPS condensates to liquid-core/gel-shell multiphase architectures through aging.[19,25]

The detection and elucidation of possible nanoscale heterogeneities in the often micrometer-sized condensate droplets are impeded by the ~300 nm resolution of diffraction-limited optical microscopy. The past decade has seen substantial advances in super-resolution microscopy (SRM), including single-molecule localization microscopy (SMLM), which, by super-localizing the positions of millions of individual molecules over consecutive camera frames, routinely achieves ~20 nm spatial resolution.[26-29] However, limited SRM applications have been demonstrated for LLPS condensates.[30-32] Moreover, intra-condensate heterogeneities may present themselves as varied local physicochemical parameters

independent of morphology or molecular distributions, which may not be resolvable by enhancing the spatial resolution alone, as will be demonstrated in our data below.

We recently developed an arsenal of *functional* SRM methods that map out physicochemical parameters at the nanoscale by tapping into the high-dimensional information space of single-molecule fluorescence.[29,33-36] Spectrally resolved SMLM (SR-SMLM) detects local parameters through the emission spectra of single probe molecules.[33-35] Single-molecule displacement/diffusivity mapping (SM*d*M) maps out diffusivity with high spatial resolutions to unveil local molecular states and interactions.[36-39] Together, these approaches have provided valuable insights into diverse cellular[34,36-39] and *in vitro*[40-42] systems.

Here we harness these technical advances to uncover nanoscale heterogeneities in the aging process of LLPS condensates, and we focus on probing the local chemical polarity, protein states, and diffusivity for the FUS system. We thus unexpectedly unveil distinct nanodomains of low chemical polarity at the condensate surfaces, and further show that these nanodomains are due to amyloid fibril aggregates and drastically impede local diffusion. Moreover, we find that such nanoaggregates progressively expand on the condensate surface upon aging or mechanical shears, thus leading to a growing low-diffusivity shell while leaving the condensate interior diffusion-permitting.

Results and discussion

SR-SMLM achieves high-throughput single-molecule spectroscopy by integrating SMLM with a wide-field dispersion scheme (Fig. 1a).[35] The resultant spectrally resolved SRM images allow functional encoding with environment-sensing probes, *e.g.*, Nile Red for probing local chemical polarity.[34,43] The solvatochromic dye Nile Red is nonfluorescent in the aqueous phase but exhibits fluorescence switch-on and spectral blueshift in hydrophobic (low chemical polarity) environments independent of the medium viscosity,[44,45] and so has been valuable for the (SR-)SMLM of lipid membranes[34,43,46] and protein aggregates.[43,47]

We employed Nile Red-based SR-SMLM to interrogate local chemical polarity in FUS condensates. To this end, we prepared wild-type and mutant FUS proteins and induced condensates following typical protocols.[11,48] Micrometer-sized droplets were formed after well-mixing the sample for 2 hr (Fig. 1b). As we allowed the condensates to settle on the coverslip and illuminated the sample with a 561 nm laser at a slanted angle slightly below the critical angle of total internal reflection,[49,50] we illuminated and imaged a cross-section of the condensate droplets ~3 μm above the coverslip surface. Stochastic local bursts of single-molecule fluorescence were observed, corresponding to individual Nile Red molecules transiently encountering a hydrophobic (low chemical polarity) phase in the sample. The wide-field fluorescence signal was split into two optical paths, with one spectrally dispersed, so single-molecule images and spectra were concurrently recorded for different molecules in the view.[34,35] Accumulating the single-molecule images and spectra over ~10^4 frames generated spectrally resolved super-resolution images (Fig. 1c), in which color presented the spectral mean of locally accumulated molecules,[34,35] hence the local chemical polarity.

We thus unveiled intriguing nanostructures in the condensates. Notably, the detected Nile Red signal highlighted discrete segments ~100 nm in apparent thickness at the condensate surface (Fig. 1c and Fig. S1). Averaging the local single-molecule spectra at these segments showed a substantial blueshift to an ~635 nm peak when compared to the ~650 nm peak averaged from the sparsely detected single-molecule signal at the condensate interior (Fig. 1d and Fig. S1). The latter value matches that found in highly hydrated environments, whereas the former blue-shifted result is consistent with the more hydrophobic environments seen at protein aggregates.[51,52] We note that for Nile Red, emission in hydrated environments at ~650 nm is sustainably weaker than in more hydrophobic environments at ~635 nm.[44] Consequently, fewer molecules were detected in the condensate interior than in the surface hydrophobic domains. However, as we illuminated the sample near total internal reflection, scattered regions of enhanced illumination were noted, attributable to local lensing effects from the likely varied refractive indices of the randomly distributed surface domains. Higher molecular counts were obtained for these regions.

Repeating Nile Red SR-SMLM over 5 days next showed that whereas the hydrophobic domains initially occurred as sporadic segments, covering ~23% of the wild-type FUS condensate surface, the surface coverage increased gradually, reaching ~60% after 3 and 5 days (Fig. 1ce and Fig. S1). The apparent thickness of this layer remained ~100 nm over the process, suggesting that the hydrophobic domains expanded laterally on the condensate surface with a fixed thickness.

We compared results with the FUS(G156E) mutant, an ALS/FTD-associated mutation known to accelerate the condensate solidification process[11,15]. We thus observed similar hydrophobic segments ~100 nm in thickness at the condensate surfaces (Fig. 1c and Fig. S2), yet noting a higher surface coverage of ~45% in the as-prepared condensates after the same initial 2 hr mixing time, and finding this coverage grew to ~80% by Day 3 and Day 5 (Fig. 1ce). The latter higher surface coverages further coincided with when the condensates started to lose their rounded shapes to become irregular in morphology, suggesting solid-like behaviors. The averaged Nile Red single-molecule spectra at the surface segments and the condensate interior (Fig. S2) were both indistinguishable from that of wild-type FUS, suggesting similar protein states.

Thus, SR-SMLM unveiled the gradual lateral expansion of ~100 nm thick hydrophobic nanodomains at the surface of FUS condensates, and this process was accelerated by the G156E mutation. Meanwhile, the condensate interior remained highly hydrated with high chemical polarity throughout the aging process.

For *in vitro* protein systems, Nile Red fluorescence switch-on and spectral blueshifts often occur at amyloid fibrils.[43,51,52] To examine this possibility, we utilized CRANAD-2 (Fig. 2a), a far-red fluorogenic probe with high affinity and specificity to amyloid fibrils.[53,54] A recent study has demonstrated CRANAD-2 for the SMLM of α-synuclein fibrils,[54] in which the stochastic amyloid binding of individual CRANAD-2 molecules gives bursts of single-molecule fluorescence.

Notably, as we applied CRANAD-2 to the FUS condensate system and performed SMLM under 642 nm excitation, we identified surface nanostructures consistent with the hydrophobic nanodomains observed above with Nile Red-based SR-SMLM. Discrete segments ~100 nm in thickness were noted at the condensate surfaces (Fig. 2b), and they similarly increased in surface coverage while maintaining their thinness when aged over days (Fig. 2bc).

As CRANAD-2 and Nile Red are spectrally distinct, we further loaded a sample with both dyes and sequentially performed SMLM for the two using their respective fluorescence filter cubes and excitation lasers. We thus found that the CRANAD-2 and Nile Red SMLM results exhibited good colocalization, both highlighting the same surface nanodomains (Fig. 2de).

Thus, with two dyes that respectively probe local chemical polarity and protein states, our SRM results indicate the gradual lateral expansion of a thin hydrophobic shell in the aging of FUS condensates through the formation of amyloid fibril aggregates.

We next inquired whether the surface aggregates we uncovered could alter local physical environments and hence the behavior of guest molecules. Here we focus on mapping molecular diffusivity, which both reflects and modulates intermolecular interactions. For this task, we turn to Cy3B (Fig. 3b), a 561-nm-excited, consistently bright dye often used in single-molecule microscopy,[55,56] contrasting with Nile Red and CRANAD-2 above only highlighting hydrophobic or amyloid phases. With a molecular weight of 560 Da, Cy3B serves as a good proxy for the mobility of similarly sized intracellular signaling molecules. Through SM*d*M, we have recently quantified the fast diffusion of this dye in water, hydrogels, and mammalian cells.[39,42]

We thus similarly prepared FUS condensates as above and added Cy3B. Epifluorescence images showed that Cy3B was ~3-fold more concentrated in the condensates versus the outside dilute phase, and this ratio stayed unvaried during aging (Fig. S3). Cy3B is moderately hydrophilic; its enhanced presence in the condensates over the dilute phase may be related to its substantially reduced diffusivity in the condensates (below).

For SM*d*M, paired stroboscopic excitation pulses were repeatedly applied in tandem across odd-even camera frames (Fig. 3a and Fig. S4), so that single-molecule images due to Cy3B molecules stochastically diffusing into the focal plane were captured, and their displacements were detected over the time window defined by the pulse separation.[36] SMLM based on the super-localized single-molecule positions over ~10^4 paired frames showed that Cy3B distributed relatively homogeneously in the droplet-like condensates at the nanoscale (Fig. 3c).

Spatially binning the accumulated single-molecule displacements with a 120 nm grid next enabled[29,36] fitting the distribution of displacements in each spatial bin to extract the local diffusion coefficient *D*. The resultant color-coded super-resolution *D* maps (Fig. 3d) and local distribution of single-molecule displacements (Fig. 3e for the region indicated by the red arrowhead in Fig. 3d) showed that the fastest diffusing regions inside the condensates reached $D \sim 10 \ \mu m^2/s$. Whereas such diffusivity would have been too fast to follow with traditional single-molecule tracking, it is only ~3% of Cy3B in water (~$340 \ \mu m^2/s$).[39,42]

We have recently shown that in hydrogels, Cy3B only exhibits mild (~15%) reductions in D at ~6 wt% polymer contents,[42] and that in mammalian cells, Cy3B diffusion is only reduced by ~25% owing to the modestly higher viscosity of the cytoplasm over water.[39] Thus, our results suggest high macromolecular crowding and/or effective viscosity for the 560 Da Cy3B in the FUS condensates. Such markedly reduced mobilities may be functionally significant for the condensates to act as concentrating hubs and interaction sites for biomolecules.[2-5]

A closer examination of the super-resolution D maps noted nanoscale segments of even greater drops in diffusivity at the condensate surface. This observation is challenging: As a 120 nm grid was implemented to warrant enough single-molecule displacements in each spatial bin for fitting, the ~100 nm thick shell we identified above at the condensate surface would be pixelated into just one or two bins in thickness. Nonetheless, facilitated by the occasionally observed nanoscale inclusions, regions with drastically reduced D of ~0.5 μm^2/s were identified (blue arrowhead in Fig. 3d inset; Fig. 3f). We also compared SMdM analysis with different grid sizes of 80, 100, and 160 nm (Fig. S4). Low-diffusivity surface domains were robustly observed; smaller grid sizes afforded higher spatial resolutions at the expense of a reduced count of single-molecule displacements in each spatial bin and thus noisier D values.

The extremely low D at the condensate surface likely corresponds to Cy3B bound to the solid-like aggregates we identified above. Indeed, as we monitored the FUS condensates over days with Cy3B SMdM, we observed that the low-diffusivity domains gradually increased their coverage at the surface (Fig. 3d and insets; Fig. S4), although quantification was difficult due to the pixelation effects.

To directly compare with surface aggregates, we added both CRANAD-2 and Cy3B to new samples, and sequentially performed SMLM and SMdM for the two dyes using their respective fluorescence filter cubes and excitation lasers. We thus found that the SMdM-resolved Cy3B slowdown regions at the condensate surface correlated well with the CRANAD-2 SMLM signal (Fig. 3g). Thus, the surface amyloid fibril aggregates are characterized by drastically lowered local diffusivities.

Diffusion inhomogeneities were also noted inside the condensates. Interestingly, the collective distribution of single-molecule displacements from the condensate interior showed two peaks (Fig. 3h for Day 0). We thus introduce a two-component fitting model to extract two D values and their respective fractions (methods). Notably, the resultant $D_1 = 9.2$ μm^2/s and $D_2 = 0.3$ μm^2/s were respectively similar to the D values observed above for the fast-diffusion regions and surface aggregates. The fraction of slow diffusion was F_2 ~15% for the as-prepared condensates. However, the SMdM data may have overrepresented the slower population, which stays better in focus between the tandem excitation pulses.

Analyzing the SMdM data of the condensate interior over aging next showed that both D_1 and D_2 remained largely unvaried (Fig. 3ik), yet the apparent fraction of the slow population gradually increased from ~15% to ~30% in 8 days (Fig. 3ij). We also examined Cy3B diffusion in the dilute phase outside the condensates and found D ~150 μm^2/s, expected with

the increased medium viscosity from dextran addition. This *D* value remained constant over 8 days (Fig. 3k), suggesting no substantial changes in the dilute-phase or medium properties in aging, so the observed changes in condensate properties were due to condensate aging *per se*.

Together, our SM*d*M results suggest that whereas the surface nanoaggregates are mostly nonmobile, the condensate interior is dominated by a fluidic phase plus a small low-diffusivity fraction. The low-diffusivity fraction likely corresponds to nanoscale aggregates inside the condensates, which, while not readily resolved in SM*d*M with the 120 nm bin sizes convolved with the different depths within the focal range, stand out through single-molecule displacement distribution analysis. Over aging, the fluidic phase maintains its liquid nature with a constant diffusivity, yet the low-diffusivity fraction steadily increases its presence, suggesting the gradual enrichment of aggregates, which may further accumulate on the condensate surface to expand the shell.

A recent study[17] has shown that mechanical shear promotes the liquid-to-solid transition of FUS condensates and results in enhanced fluorescence of Thioflavin T, a common amyloid probe. To test if this behavior could be related to our above-observed gradual formation of amyloid-like aggregates at the FUS condensate surface in aging, we prepared FUS LLPS samples in which we imposed mechanical shear by repeated pipetting.

For samples pipetted 20 times, we thus observed significantly increased coverage of amyloid nanoaggregates at the FUS condensate surface, as visualized by the colocalization of CRANAD-2 SMLM signal and reduced local diffusivity of Cy3B in the SM*d*M *D* map (Fig. 4a). Quantification indicated that the CRANAD-2 SMLM signal covered ~60% of the condensate surface (Fig. 4c), substantially higher than that of the non-agitated samples (Fig. 2c) as prepared (~20%) or aged for 4 days (~50%). Moreover, irregular-shaped nanoaggregates were noted extruding out of the condensate surface (arrows in Fig. 4a).

For samples pipetted 200 times, the condensates lost their droplet-like rounded shapes, but appeared as granules of irregular shapes. Interestingly, CRANAD-2 SMLM (Fig. 4b) showed high coverage of the granule surfaces to form a shell thickened to ~400 nm, yet signal from the granule interior remained low, except for aggregate intrusions from the surface (arrow in Fig. 4b). Meanwhile, Cy3B SM*d*M showed impeded diffusion for a thickened shell that corresponded well with the CRANAD-2 SMLM signal (Fig. 4b). Notably, diffusion at the granule interior remained reasonably fast at $>$~5 μm^2/s (Fig. 4b), suggesting that a liquid-liked core remained even as the granule surface was covered by a thickened shell of amyloid aggregates. The thickened amyloid-aggregate shell versus the ~100 nm thick layer in unagitated aging may be related to the observed extrusions and intrusions, which likely caused further exposure of the condensate interior and accumulation of aggregates.

Conclusions

To sum, harnessing a set of multidimensional SRM tools, we unveiled nanoscale heterogeneity in FUS condensates, identifying hydrophobic amyloid aggregates at the

condensate surface, showing their substantial suppression of local diffusivity, and elucidating their gradual expansion during aging.

For the LLPS of a single protein, one may intuitively assume each condensate microdroplet as a uniform phase. However, recent theories point to the possible gradual transformation of initially homogenous FUS LLPS condensates to a liquid-core/gel-shell architecture through aging.[25] A new experimental study supported this notion for the non-agitated aging of FUS condensates, suggesting the gradual solidification of the condensate surface over several days through a dissolution assay.[19] Separately, tracing individual gold nanorods in TFEB condensates has indicated reduced mobilities at the condensate surface.[57] However, these recent discoveries have not uncovered the existence of nanoscale surface domains or identified their amyloid fibril nature.

In this study, we uncovered nanoscale amyloid fibril aggregates at the condensate surface, and showed that over aging, such nanoaggregates gradually expanded at the surface and increased their intra-condensate presence (model in Fig. 4d). These findings benefited from both the high spatial resolution and the multidimensional insights afforded by our approaches: Indeed, SMLM of Cy3B showed relatively uniform spatial distribution in the condensates, but SM*d*M of the same dye showed drastically impeded diffusion at the surface nanoaggregates, and SR-SMLM with Nile Red highlighted their hydrophobic nature and prompted us to employ CRANAD-2 SMLM to identify their amyloid state.

The low-complexity domains of FUS are known to drive both LLPS and fibril formation.[11,12,58-63] As FUS molecules aggregate into the fibril state, their low-complexity domains are buried into a hydrophobic core, as detected by our Nile Red SR-SMLM. It is thus likely that the aggregated molecules no longer participate in the LLPS interactions and so are excluded from the condensate interior. Under this scenario, the preferred structures formed by the immiscible condensate and fibril phases may be explained by the relative surface tensions at the different interfaces.[3,64] Our observed ~100 nm-thick fibril nanodomains suggest that the condensate surface is a heterogenous environment where aggregates accumulate, with our SM*d*M and SMLM data further signifying their functional implications as local diffusion barriers and rigidification loci. Meanwhile, the observed gradual expansion of amyloid fibril nanoaggregates during aging, as well as their markedly enhanced formation upon repeated pipetting, suggest that while the LLPS condensates are initially fast formed under kinetic control, the fibril state is energetically favored as the system evolves toward equilibrium.

Together, our results unveiled unexpected nanoscale structural arrangements and aging mechanisms for the single-component FUS condensates with exceptional spatial and functional insights. Generalizing the multidimensional SRM approaches demonstrated in this work to other LLPS systems to uncover related, or yet other unknown, behaviors at the nanoscale presents exciting opportunities.

Supplementary Material

Refer to Web version on PubMed Central for supplementary material.

Acknowledgments

Reference

(1). Hyman AA; Weber CA; Julicher F Liquid-liquid phase separation in biology. Annu Rev Cell Dev Biol 2014, 30, 39–58. [PubMed: 25288112]

(2). Banani SF; Lee HO; Hyman AA; Rosen MK Biomolecular condensates: organizers of cellular biochemistry. Nat. Rev. Mol. Cell Biol 2017, 18, 285–298. [PubMed: 28225081]

(3). Shin Y; Brangwynne CP Liquid phase condensation in cell physiology and disease. Science 2017, 357, eaaf4382. [PubMed: 28935776]

(4). Alberti S; Gladfelter A; Mittag T Considerations and Challenges in Studying Liquid-Liquid Phase Separation and Biomolecular Condensates. Cell 2019, 176, 419–434. [PubMed: 30682370]

(5). Lyon AS; Peeples WB; Rosen MK A framework for understanding the functions of biomolecular condensates across scales. Nat. Rev. Mol. Cell Biol 2021, 22, 215–235. [PubMed: 33169001]

(6). Li P; Banjade S; Cheng HC; Kim S; Chen B; Guo L; Llaguno M; Hollingsworth JV; King DS; Banani SF et al. Phase transitions in the assembly of multivalent signalling proteins. Nature 2012, 483, 336–340. [PubMed: 22398450]

(7). Su X; Ditlev JA; Hui E; Xing W; Banjade S; Okrut J; King DS; Taunton J; Rosen MK; Vale RD Phase separation of signaling molecules promotes T cell receptor signal transduction. Science 2016, 352, 595–599. [PubMed: 27056844]

(8). Larson AG; Elnatan D; Keenen MM; Trnka MJ; Johnston JB; Burlingame AL; Agard DA; Redding S; Narlikar GJ Liquid droplet formation by HP1α suggests a role for phase separation in heterochromatin. Nature 2017, 547, 236–240. [PubMed: 28636604]

(9). Chong S; Dugast-Darzacq C; Liu Z; Dong P; Dailey GM; Cattoglio C; Heckert A; Banala S; Lavis L; Darzacq X et al. Imaging dynamic and selective low-complexity domain interactions that control gene transcription. Science 2018, 361, eaar2555. [PubMed: 29930090]

(10). Sabari BR; Dall'Agnese A; Boija A; Klein IA; Coffey EL; Shrinivas K; Abraham BJ; Hannett NM; Zamudio AV; Manteiga JC et al. Coactivator condensation at super-enhancers links phase separation and gene control. Science 2018, 361, eaar3958. [PubMed: 29930091]

(11). Patel A; Lee HO; Jawerth L; Maharana S; Jahnel M; Hein MY; Stoynov S; Mahamid J; Saha S; Franzmann TM et al. A Liquid-to-Solid Phase Transition of the ALS Protein FUS Accelerated by Disease Mutation. Cell 2015, 162, 1066–1077. [PubMed: 26317470]

(12). Murakami T; Qamar S; Lin JQ; Schierle GS; Rees E; Miyashita A; Costa AR; Dodd RB; Chan FT; Michel CH et al. ALS/FTD Mutation-Induced Phase Transition of FUS Liquid Droplets and Reversible Hydrogels into Irreversible Hydrogels Impairs RNP Granule Function. Neuron 2015, 88, 678–690. [PubMed: 26526393]

(13). Qamar S; Wang G; Randle SJ; Ruggeri FS; Varela JA; Lin JQ; Phillips EC; Miyashita A; Williams D; Strohl F et al. FUS Phase Separation Is Modulated by a Molecular Chaperone and Methylation of Arginine Cation-pi Interactions. Cell 2018, 173, 720–734. [PubMed: 29677515]

(14). Wang J; Choi JM; Holehouse AS; Lee HO; Zhang X; Jahnel M; Maharana S; Lemaitre R; Pozniakovsky A; Drechsel D et al. A Molecular Grammar Governing the Driving Forces for Phase Separation of Prion-like RNA Binding Proteins. Cell 2018, 174, 688–699. [PubMed: 29961577]

(15). Rhine K; Makurath MA; Liu J; Skanchy S; Lopez C; Catalan KF; Ma Y; Fare CM; Shorter J; Ha T et al. ALS/FTLD-Linked Mutations in FUS Glycine Residues Cause Accelerated Gelation and Reduced Interactions with Wild-Type FUS. Mol. Cell 2020, 80, 666–681. [PubMed: 33159856]

(16). Jawerth L; Fischer-Friedrich E; Saha S; Wang J; Franzmann T; Zhang X; Sachweh J; Ruer M; Ijavi M; Saha S et al. Protein condensates as aging Maxwell fluids. Science 2020, 370, 1317–1323. [PubMed: 33303613]

(17). Shen Y; Ruggeri FS; Vigolo D; Kamada A; Qamar S; Levin A; Iserman C; Alberti S; St George-Hyslop P; Knowles TPJ Biomolecular condensates undergo a generic shear-mediated liquid-to-solid transition. Nat. Nanotechnol 2020, 15, 841–847. [PubMed: 32661370]

(18). Portz B; Lee BL; Shorter J FUS and TDP-43 Phases in Health and Disease. Trends Biochem Sci 2021, 46, 550–563. [PubMed: 33446423]

(19). Shen Y; Chen A; Wang W; Shen Y; Ruggeri FS; Aime S; Wang Z; Qamar S; Espinosa JR; Garaizar A et al. The liquid-to-solid transition of FUS is promoted by the condensate surface. Proc. Natl. Acad. Sci. U. S. A 2023, 120, e2301366120. [PubMed: 37549257]

(20). Molliex A; Temirov J; Lee J; Coughlin M; Kanagaraj AP; Kim HJ; Mittag T; Taylor JP Phase separation by low complexity domains promotes stress granule assembly and drives pathological fibrillization. Cell 2015, 163, 123–133. [PubMed: 26406374]

(21). Wegmann S; Eftekharzadeh B; Tepper K; Zoltowska KM; Bennett RE; Dujardin S; Laskowski PR; MacKenzie D; Kamath T; Commins C et al. Tau protein liquid-liquid phase separation can initiate tau aggregation. EMBO J 2018, 37, e98049. [PubMed: 29472250]

(22). Kanaan NM; Hamel C; Grabinski T; Combs B Liquid-liquid phase separation induces pathogenic tau conformations in vitro. Nat. Commun 2020, 11, 2809. [PubMed: 32499559]

(23). Babinchak WM; Haider R; Dumm BK; Sarkar P; Surewicz K; Choi JK; Surewicz WK The role of liquid-liquid phase separation in aggregation of the TDP-43 low-complexity domain. J. Biol. Chem 2019, 294, 6306–6317. [PubMed: 30814253]

(24). Ray S; Singh N; Kumar R; Patel K; Pandey S; Datta D; Mahato J; Panigrahi R; Navalkar A; Mehra S et al. α-Synuclein aggregation nucleates through liquid-liquid phase separation. Nat. Chem 2020, 12, 705–716. [PubMed: 32514159]

(25). Garaizar A; Espinosa JR; Joseph JA; Krainer G; Shen Y; Knowles TPJ; Collepardo-Guevara R Aging can transform single-component protein condensates into multiphase architectures. Proc. Natl. Acad. Sci. U. S. A 2022, 119, e2119800119. [PubMed: 35727989]

(26). Sigal YM; Zhou R; Zhuang X Visualizing and discovering cellular structures with super-resolution microscopy. Science 2018, 361, 880–887. [PubMed: 30166485]

(27). Möckl L; Moerner WE Super-resolution microscopy with single molecules in biology and beyond-essentials, current trends, and future challenges. J. Am. Chem. Soc 2020, 142, 17828–17844. [PubMed: 33034452]

(28). Lelek M; Gyparaki MT; Beliu G; Schueder F; Griffié J; Manley S; Jungmann R; Sauer M; Lakadamyali M; Zimmer C Single-molecule localization microscopy. Nat. Rev. Methods Primers 2021, 1, 39. [PubMed: 35663461]

(29). Xiang L; Chen K; Xu K Single molecules are your quanta: A bottom-up approach toward multidimensional super-resolution microscopy. ACS Nano 2021, 15, 12483–12496. [PubMed: 34304562]

(30). Fei J; Jadaliha M; Harmon TS; Li ITS; Hua B; Hao Q; Holehouse AS; Reyer M; Sun Q; Freier SM et al. Quantitative analysis of multilayer organization of proteins and RNA in nuclear speckles at super resolution. J. Cell Sci 2017, 130, 4180–4192. [PubMed: 29133588]

(31). Fasciani A; D'Annunzio S; Poli V; Fagnocchi L; Beyes S; Michelatti D; Corazza F; Antonelli L; Gregoretti F; Oliva G et al. MLL4-associated condensates counterbalance Polycomb-mediated nuclear mechanical stress in Kabuki syndrome. Nat Genet 2020, 52, 1397–1411. [PubMed: 33169020]

(32). Zhang HC; Shao SP; Zeng Y; Wang XT; Qin YZ; Ren QN; Xiang SQ; Wang YX; Xiao JY; Sun YJ Reversible phase separation of HSF1 is required for an acute transcriptional response during heat shock. Nat. Cell Biol 2022, 24, 340–352. [PubMed: 35256776]

(33). Zhang Z; Kenny SJ; Hauser M; Li W; Xu K Ultrahigh-throughput single-molecule spectroscopy and spectrally resolved super-resolution microscopy. Nat. Methods 2015, 12, 935–938. [PubMed: 26280329]

(34). Moon S; Yan R; Kenny SJ; Shyu Y; Xiang L; Li W; Xu K Spectrally resolved, functional super-resolution microscopy reveals nanoscale compositional heterogeneity in live-cell membranes. J. Am. Chem. Soc 2017, 139, 10944–10947. [PubMed: 28774176]

(35). Yan R; Moon S; Kenny SJ; Xu K Spectrally resolved and functional super-resolution microscopy via ultrahigh-throughput single-molecule spectroscopy. Acc. Chem. Res 2018, 51, 697–705. [PubMed: 29443498]

(36). Xiang L; Chen K; Yan R; Li W; Xu K Single-molecule displacement mapping unveils nanoscale heterogeneities in intracellular diffusivity. Nat. Methods 2020, 17, 524–530. [PubMed: 32203387]

(37). Yan R; Chen K; Xu K Probing nanoscale diffusional heterogeneities in cellular membranes through multidimensional single-molecule and super-resolution microscopy. J. Am. Chem. Soc 2020, 142, 18866–18873. [PubMed: 33084318]

(38). Xiang L; Yan R; Chen K; Li W; Xu K Single-molecule displacement mapping unveils sign-asymmetric protein charge effects on intraorganellar diffusion. Nano Lett. 2023, 23, 1711–1716. [PubMed: 36802676]

(39). Choi AA; Xiang L; Li W; Xu K Single-molecule displacement mapping indicates unhindered intracellular diffusion of small (≤1 kDa) solutes. J. Am. Chem. Soc 2023, 145, 8510–8516.

(40). Xiang L; Wojcik M; Kenny SJ; Yan R; Moon S; Li W; Xu K Optical characterization of surface adlayers and their compositional demixing at the nanoscale. Nat. Commun 2018, 9, 1435. [PubMed: 29650981]

(41). Choi AA; Park HH; Chen K; Yan R; Li W; Xu K Displacement statistics of unhindered single molecules show no enhanced diffusion in enzymatic reactions. J. Am. Chem. Soc 2022, 144, 4839–4844. [PubMed: 35258969]

(42). Park HH; Choi AA; Xu K Size-dependent suppression of molecular diffusivity in expandable hydrogels: A single-molecule study. J. Phys. Chem. B 2023, 127, 3333–3339. [PubMed: 37011131]

(43). Bongiovanni MN; Godet J; Horrocks MH; Tosatto L; Carr AR; Wirthensohn DC; Ranasinghe RT; Lee JE; Ponjavic A; Fritz JV et al. Multi-dimensional super-resolution imaging enables surface hydrophobicity mapping. Nat. Commun 2016, 7, 13544. [PubMed: 27929085]

(44). Sackett DL; Wolff J Nile red as a polarity-sensitive fluorescent probe of hydrophobic protein surfaces. Anal. Biochem 1987, 167, 228–234. [PubMed: 3442318]

(45). Cser A; Nagy K; Biczók L Fluorescence lifetime of Nile Red as a probe for the hydrogen bonding strength with its microenvironment. Chem. Phys. Lett 2002, 360, 473–478.

(46). Sharonov A; Hochstrasser RM Wide-field subdiffraction imaging by accumulated binding of diffusing probes. Proc. Natl. Acad. Sci. U. S. A 2006, 103, 18911–18916. [PubMed: 17142314]

(47). Lee JE; Sang JC; Rodrigues M; Carr AR; Horrocks MH; De S; Bongiovanni MN; Flagmeier P; Dobson CM; Wales DJ et al. Mapping surface hydrophobicity of α-synuclein oligomers at the nanoscale. Nano Lett. 2018, 18, 7494–7501. [PubMed: 30380895]

(48). Alberti S; Saha S; Woodruff JB; Franzmann TM; Wang J; Hyman AA A User's Guide for Phase Separation Assays with Purified Proteins. J Mol Biol 2018, 430, 4806–4820. [PubMed: 29944854]

(49). Cui B; Wu C; Chen L; Ramirez A; Bearer EL; Li W-P; Mobley WC; Chu S One at a time, live tracking of NGF axonal transport using quantum dots. Proc. Natl. Acad. Sci. U. S. A 2007, 104, 13666–13671. [PubMed: 17698956]

(50). Tokunaga M; Imamoto N; Sakata-Sogawa K Highly inclined thin illumination enables clear single-molecule imaging in cells. Nat. Methods 2008, 5, 159–161. [PubMed: 18176568]

(51). Mishra R; Sjolander D; Hammarstrom P Spectroscopic characterization of diverse amyloid fibrils in vitro by the fluorescent dye Nile red. Mol Biosyst 2011, 7, 1232–1240. [PubMed: 21279219]

(52). Krishnan R; Goodman JL; Mukhopadhyay S; Pacheco CD; Lemke EA; Deniz AA; Lindquist S Conserved features of intermediates in amyloid assembly determine their benign or toxic states. Proc. Natl. Acad. Sci. U. S. A 2012, 109, 11172–11177. [PubMed: 22745165]

(53). Ran C; Xu X; Raymond SB; Ferrara BJ; Neal K; Bacskai BJ; Medarova Z; Moore A Design, Synthesis, and Testing of Difluoroboron-Derivatized Curcumins as Near-Infrared Probes for in Vivo Detection of Amyloid-β Deposits. J. Am. Chem. Soc 2009, 131, 15257–15261. [PubMed: 19807070]

(54). Torra J; Viela F; Megias D; Sot B; Flors C Versatile Near-Infrared Super-Resolution Imaging of Amyloid Fibrils with the Fluorogenic Probe CRANAD-2. Chem. Eur. J 2022, 28, e202200026. [PubMed: 35178798]

(55). Cooper M; Ebner A; Briggs M; Burrows M; Gardner N; Richardson R; West R Cy3B™: Improving the Performance of Cyanine Dyes. J. Fluorescence 2004, 14, 145–150.

(56). Ha T; Tinnefeld P Photophysics of fluorescent probes for single-molecule biophysics and super-resolution imaging. Annu. Rev. Phys. Chem 2012, 63, 595–617. [PubMed: 22404588]

(57). Wang Z; Chen D; Guan D; Liang X; Xue J; Zhao H; Song G; Lou J; He Y; Zhang H Material properties of phase-separated TFEB condensates regulate the autophagy-lysosome pathway. J. Cell Biol 2022, 221, e202112024. [PubMed: 35293953]

(58). Kato M; Han TW; Xie S; Shi K; Du X; Wu LC; Mirzaei H; Goldsmith EJ; Longgood J; Pei J et al. Cell-free formation of RNA granules: low complexity sequence domains form dynamic fibers within hydrogels. Cell 2012, 149, 753–767. [PubMed: 22579281]

(59). Burke KA; Janke AM; Rhine CL; Fawzi NL Residue-by-Residue View of In Vitro FUS Granules that Bind the C-Terminal Domain of RNA Polymerase II. Mol. Cell 2015, 60, 231–241. [PubMed: 26455390]

(60). Murray DT; Kato M; Lin Y; Thurber KR; Hung I; McKnight SL; Tycko R Structure of FUS Protein Fibrils and Its Relevance to Self-Assembly and Phase Separation of Low-Complexity Domains. Cell 2017, 171, 615–627. [PubMed: 28942918]

(61). Hughes MP; Sawaya MR; Boyer DR; Goldschmidt L; Rodriguez JA; Cascio D; Chong L; Gonen T; Eisenberg DS Atomic structures of low-complexity protein segments reveal kinked beta sheets that assemble networks. Science 2018, 359, 698–701. [PubMed: 29439243]

(62). Luo F; Gui X; Zhou H; Gu J; Li Y; Liu X; Zhao M; Li D; Li X; Liu C Atomic structures of FUS LC domain segments reveal bases for reversible amyloid fibril formation. Nat. Struct. Mol. Biol 2018, 25, 341–346. [PubMed: 29610493]

(63). Murthy AC; Dignon GL; Kan Y; Zerze GH; Parekh SH; Mittal J; Fawzi NL Molecular interactions underlying liquid-liquid phase separation of the FUS low-complexity domain. Nat. Struct. Mol. Biol 2019, 26, 637–648. [PubMed: 31270472]

(64). Gouveia B; Kim Y; Shaevitz JW; Petry S; Stone HA; Brangwynne CP Capillary forces generated by biomolecular condensates. Nature 2022, 609, 255–264. [PubMed: 36071192]
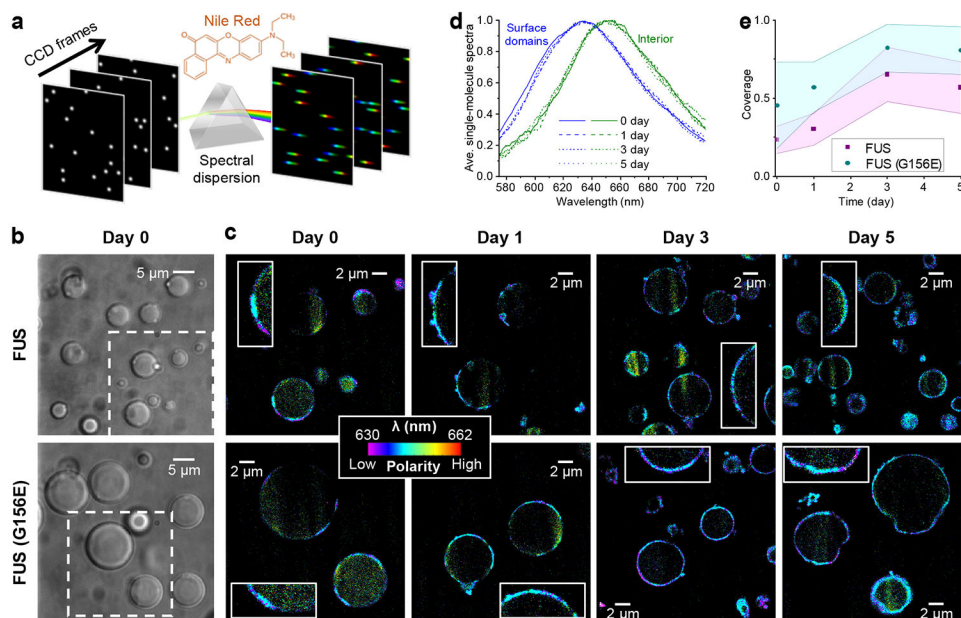
Figure 1.

SR-SMLM with Nile Red unveils growing hydrophobic (low chemical polarity) nanodomains at the FUS condensate surface. **a**. Schematics: Single-molecule fluorescence is spectrally dispersed in the wide field, and the resultant single-molecule spectra are accumulated over many camera frames to generate SR-SMLM images. **b**. Brightfield micrographs of condensates formed by wild-type (top) and G156E-mutant (bottom) FUS. **c**. Nile Red SR-SMLM images for FUS (top) and FUS(G156E) (bottom) condensates aged for different days. Color presents the mean wavelength of the local single-molecule spectra (color scale bar), which reflects the local chemical polarity. The Day 0 images correspond to the boxed regions in (b). Insets: Zoom-ins of the condensate surfaces, highlighting the hydrophobic nanodomains. **d**. Averaged single-molecule spectra at the condensate surface hydrophobic domains (blue) and the condensate interior (green), for FUS condensates aged for different days (different line shapes). **e**. Time-dependent surface coverage of the Nile Red-visualized hydrophobic domains over aging. Data points and shades present the averages and standard deviations of individual condensate droplets (~10 for each data point), respectively.
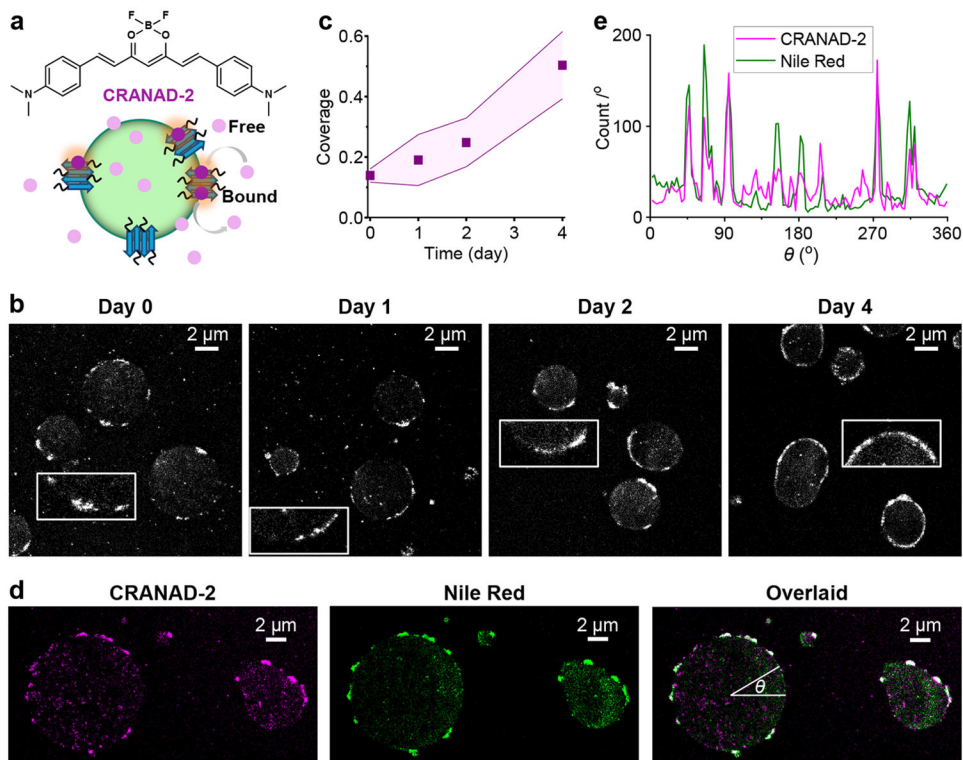
Figure 2.
SMLM with CRANAD-2 indicates the gradual formation of amyloid fibril nanoaggregates at the FUS condensate surface. **a**. CRANAD-2 chemical structure and mode of action: CRANAD-2 is nonfluorescent in the aqueous phase but turns on fluorescence upon binding to amyloid fibrils in the condensates. **b**. Representative SMLM images of CRANAD-2, for FUS condensates aged for different days. Insets: Zoom-ins highlighting the surface nanodomains. **c**. Time-dependent surface coverage of CRANAD-2 SMLM signal at FUS condensates over aging. Data points and shades present the averages and standard deviations of individual condensates (~10 for each data point), respectively. **d**. Two-color SMLM for a FUS LLPS sample loaded with both CRANAD-2 and Nile Red, shown as separate (CRANAD-2: magenta, Nile Red: green) and overlaid (colocalization: white) images. **e**. Line profiles of single-molecule localizations in the two dye channels along the circumference of a condensate droplet, presented as counts per degree as a function of the azimuth angle θ marked in (d).
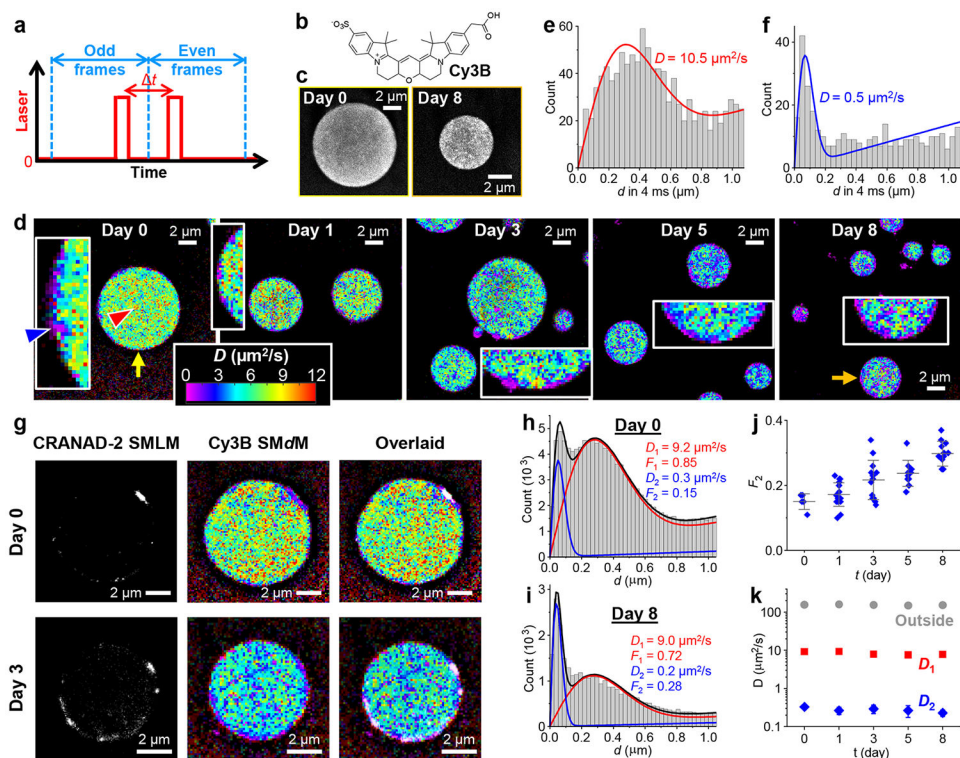
Figure 3.
SM*d*M with Cy3B shows impeded diffusion in the FUS condensates and further large drops in diffusivity at the surface aggregates. **a**. Scheme of SM*d*M. Paired stroboscopic excitation pulses are repeatedly applied in tandem across odd-even camera frames, so that single-molecule displacements are captured for the time window defined by the separation between the tandem pulses *t* rather than the camera framerate. **b**. Chemical structure of Cy3B. **c**. SMLM images based on the localized positions of Cy3B molecules in the SM*d*M data, for FUS condensates as prepared (left) and aged for 8 days (right). **d**. Color-coded SM*d*M super-resolution *D* maps of Cy3B in FUS condensates aged for different days, obtained by spatially binning the accumulated single-molecule displacements onto a 120 nm grid, and then fitting the distribution in each bin to extract the local *D* for color rendering. The condensates indicated by the yellow and orange arrows correspond to the ones shown in (c). Insets: zoom-ins of the condensate surfaces, highlighting local diffusion slowdowns. **e,f**. Histograms: Local distributions of the accumulated single-molecule displacements at *t* = 4 ms, for two regions pointed to by the red and blue arrowheads in (d), respectively. Red and blue curves: Fits to our diffusion model, with resultant *D* values marked in the plots. **g**. Sequentially acquired CRANAD-2 SMLM images and Cy3B SM*d*M *D* maps for FUS condensates as-prepared (top) and aged 3 days (bottom), shown as separated and overlaid images. **h,i**. Two-component fits (red curve: fast component; blue curve: slow component; black curve: sum) to the single-molecule displacements (histograms) collected at the FUS-condensate interior at Day 0 (top) and Day 8 (bottom). Resultant *D* values and fractions of the two components are marked in the plots. **j**. Fraction of the low-diffusivity component, as obtained above, for the interior of FUS condensates aged for different days. Each data point corresponds to one individual condensate. **k**. Fitted *D* values for the fast (red) and slow

(blue) components, as obtained above, for the interior of FUS condensates aged for different days, versus D values in the dilute phase outside the condensates (gray). Error bars in (j,k): standard deviations between individual condensates.
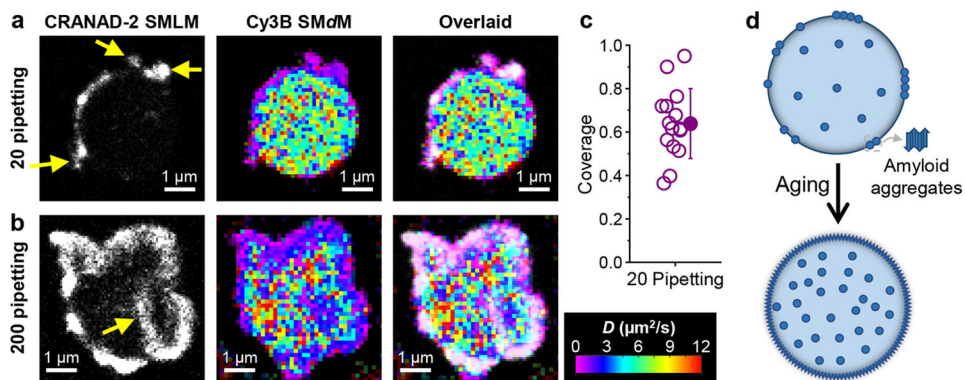
Figure 4.

Mechanical shear induces similar amyloid fibril aggregates at the FUS condensate surface. **a,b**. Sequentially acquired CRANAD-2 SMLM images and Cy3B SM*d*M *D* maps, and overlaid images, for FUS condensates subjected to 20 (a) and 200 (b) times of pipetting. Arrows in (a,b) point to extrusions and intrusions of the surface aggregates. **c**. Surface coverage of CRANAD-2 SMLM signal for FUS condensates pipetted 20 times. Open circles: Individual condensates. Filled circle and error bar: Average and standard deviation. **d**. Model: Enrichment of amyloid aggregates in the condensates and accumulation at the surface during aging.